Universal Dripping and Jetting in a Transverse Shear Flow

Robert F. Meyer and John C. Crocker*

Department of Chemical and Biomolecular Engineering, University of Pennsylvania, 220 South 33rd Street, Philadelphia, Pennsylvania 19104-6393, USA

(Received 12 December 2008; published 12 May 2009)

One particularly efficient approach to making emulsions having monosized droplets is to push a fluid through an orifice into a transverse flow of a second immiscible fluid. We find that, at an intermediate particle Reynolds number, the final droplet size can be readily computed using a simple force balance. Remarkably like the well-known dripping faucet, this system displays both dripping and jetting behavior, controlled by the capillary, Weber and Ohnesorge numbers of the relevant fluids, and interesting nonlinear behavior such as period doubling near the transition between these two regimes.

DOI: 10.1103/PhysRevLett.102.194501 PACS numbers: 47.55.db, 47.60.Kz, 47.61.Jd

Drop formation and breakup have long been an object of interest due to the surprising complexity of the phenomena [1]. Breakup occurs either by an external force tearing a growing drop from an orifice, as in the dripping faucet, or at higher flow rates, by the breakup of a jet emerging from the orifice, as in the Rayleigh instability [2]. Near the transition between dripping and jetting, drop formation shows interesting nonlinear dynamics, including period doubling and chaos [3,4]. More recent studies have probed drop formation in several microfluidic geometries, such as coaxial flow [5,6] and T junctions [7], where controlled droplet formation is an important technological problem.

Here we study droplet formation in a cross-flow membrane emulsification (XME) geometry, a high-throughput method for generating monodisperse droplets [8–10]. In XME, the dispersed phase (DP) is forced through an orifice in a planar membrane into a simple shear flow set up by a second continuous phase (CP) flowing parallel to the membrane surface; see Fig. 1(a). In the dripping regime, when buoyancy forces are negligible [11], the final droplet diameter D results from the competition between hydrodynamic stresses proportional to the CP shear rate $\frac{dv}{dz}$ and forces from the interfacial tension γ. This leads us to introduce the capillary number, which is a ratio of a drag force $\mu_{\mathrm{CP}} \frac{dv}{dz} D_0^2$ and an interfacial tension force γD_0: $\mathrm{Ca} = \mu_{\mathrm{CP}} \frac{dv}{dz} D_0/\gamma$, where μ is the viscosity and D_0 the orifice diameter. At high DP flow rates, the inertial force of the fluid emerging from the orifice $\rho_{\mathrm{DP}} Q_{\mathrm{DP}}^2/D_0^2$ exceeds the interfacial tension force, leading to a transition to jetting behavior, where Q is the volumetric flow rate and ρ the mass density. The ratio of these forces is the Weber number: $\mathrm{We} = \rho_{\mathrm{DP}} Q_{\mathrm{DP}}^2/D_0^3\gamma$. We find that the droplet size in the dripping regime scales with the applied forces in a manner different from those in the dripping faucet and coaxial flow geometries but that the transition between dripping and jetting is remarkably similar. This latter point is more surprising given the lack of axial symmetry in our system.

Our experimental apparatus consists of a long rectangular channel with height $H = 3.2$ mm and width $W = 6.4$ mm through which the CP flows. The DP is forced through a single circular pore ($D_0 = 15$, 90, or 132 μm) on the center line of the bottom wall, using a syringe pump. Drop formation is monitored from the side, with a viewing angle 7° above the membrane plane, using a long-working distance video microscope. A pair of right angle prisms straddling the channel redirects illumination and viewing light through a window at the top of the channel. Several fluids were used for the DP, listed in Table I, while the CP was limited to water, sometimes with poly(vinyl alcohol) (PVA) as a surfactant. For each system studied, the two fluids were equilibrated in contact, so as to minimize mass transfer during the experiment. The densities ρ_{CP} and ρ_{DP}, viscosities μ_{CP} and μ_{DP}, and interfacial tension γ for each equilibrated combination were measured directly by mass, capillary viscometry, and pendant drop profilometry [13], respectively (cf. Table I).

The qualitative features of the dripping and jetting behavior in XME are shown by the images in Fig. 1, taken at a constant Ca. At low Weber number $\mathrm{We} = 0.5$, simple dripping is observed [Figs. 1(b)–1(d)]. Because the interfacial force is dominant, the droplet is able to grow reproducibly each cycle until detached by the flowing CP. At $\mathrm{We} = 1.1$, the location of droplet snap-off moves away from the orifice, but the size of the resultant droplet remains roughly the same [Figs. 1(e)–1(g)]. The momentum of the flowing DP distends the droplet neck noticeably; for these parameters, the distended neck also snaps off reproducibly to form a satellite droplet. Increasing the DP flow rate further by 20%, $\mathrm{We} = 1.6$, causes further extension of the droplet neck, with multiple peaks and nodes observed, and a noticeable decrease in droplet size [Figs. 1(h)–1(j)]. An additional 10% increase in Q_{DP}, $\mathrm{We} = 2.0$, leads to a stable bifurcation of the resultant droplet size, where the elongated neck or jet alternates production of small and large droplets [Figs. 1(k)–1(m)]. These and more complex nonlinear dynamical behavior (not shown) were observed

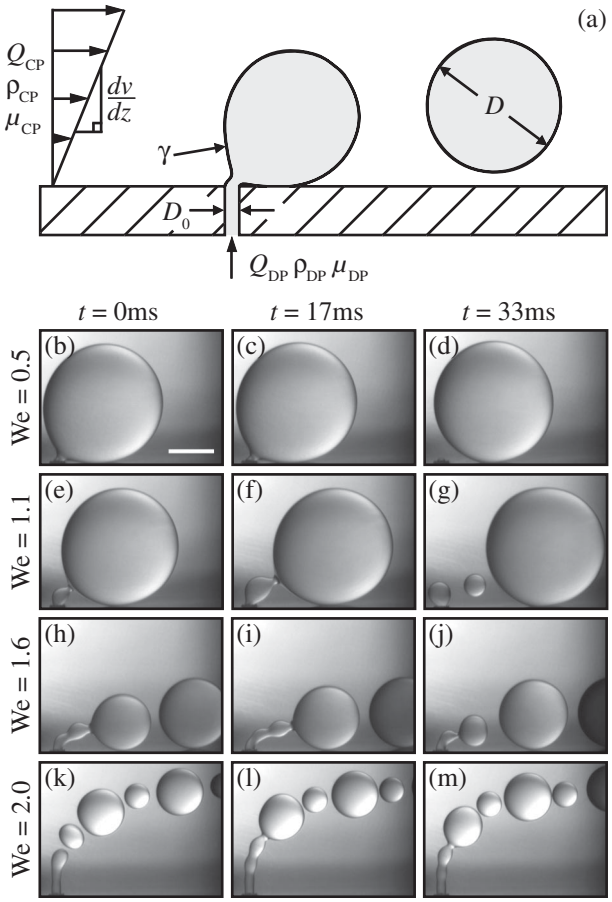

FIG. 1. Dripping and jetting at various We for $\mathrm{Ca} = 8 \times 10^{-4}$ and $\mathrm{Oh}_{DP} = 4 \times 10^{-2}$, variables defined in text. (a) Cartoon representation of the XME process, where droplets of DP are torn from an orifice by a simple shear flow in the CP. At low DP flow rates, monodisperse drops form and break off near the pore (b)–(d); scale bar = 500 μm. As the DP flow is increased, the first droplets are the same size but move away from the pore prior to snap-off, forming satellite drops (e)–(g). Eventually, the fluid neck lengthens further and droplet sizes decrease (h)–(j). Ultimately, a bent fluid jet breaks into droplets, exhibiting period doubling (k)–(m).

near the transition, over the entire range of different Ca we studied.

Given the interest in using XME to produce monodisperse emulsions, we first seek to understand the particle size in the dripping regime (i.e., low We), as a function of the hydrodynamic stress due to the shear flow; typical data are shown in Fig. 2(a). For all systems studied, the droplet diameter scales as $D \propto \frac{dv}{dz}^{-1/2}$. This square root dependence has a simple physical origin. In our geometry, the mean velocity of the fluid at the drop center is itself proportional to the droplet size, as larger droplets poke up higher to impinge on faster flows, leading the hydrodynamic stress to depend quadratically on the droplet diameter. Equating that hydrodynamic stress with a constant, maximal interfacial tension at snap-off trivially yields the desired scaling exponent.

TABLE I. Liquids used and their physical properties at 18 °C. Mixture proportions are given in w/w. Small, medium, and large symbols represent a D_0 of 15, 90, or 132 μm, respectively.

Dispersed phase (surfactant)	ρ_{DP} (kg/m^3)	μ_{DP} (mPa s)	γ (mN/m)	Symbol
n-butanol	827	3.31	2.4	◇
n-pentanol	817	3.61	4.8	□
n-hexanol	809	5.06	6.3	○
DCM[a] +hexanol 20/80	871	3.12	7.5	⊕
DCM + hexanol 40/60	943	1.79	9.7	⊗
DCM + hexanol 60/40	1039	1.14	9.1	⊙
DCM (0.05% PVA)	1320	0.44	12.0	△
DCM (0.5% PVA)	1320	0.44	6.1	▽
DCM (0.5% PVA)[b]	1320	0.44	6.1	☆
Ethyl acetate	902	0.50	6.5	▷

[a]Dichloromethane.
[b]Computational fluid dynamics simulation [12].

To make such a force-balance relation more precise, we begin by equating the drag force F_d with the interfacial tension force F_γ at the moment of snap-off:

$$F_d = \frac{\pi}{8} C_d \rho_{CP} v_\infty^2 D^2 = F_\gamma = \pi D_0 \gamma, \qquad (1)$$

where v_∞ is the far-field velocity at the droplet midline and $C_d = C_d(\mathrm{Re}_p, \lambda)$ is the drag coefficient for a spherical droplet with particle Reynolds number $\mathrm{Re}_p = \rho_{CP} v_\infty D/\mu_{CP}$ and viscosity ratio $\lambda = \mu_{DP}/\mu_{CP}$.

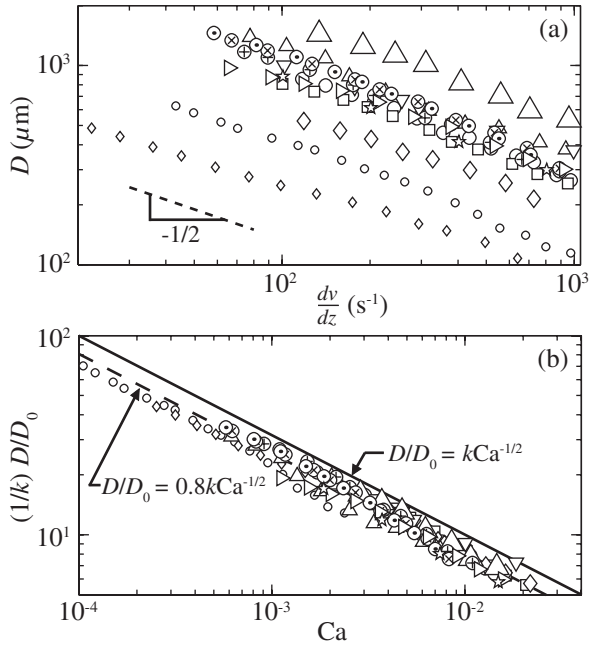

FIG. 2. (a) Droplet diameter D versus shear rate $\frac{dv}{dz}$ for all fluid systems. (b) Collapse of scaled droplet size $(1/k)D/D_0$ as a function of Ca, with k calculated from Eq. (3). The collapsed experimental data fall roughly 20% lower than the force-balance prediction (solid line), comparable to results from computational fluid dynamics (☆). See Table I for symbol definitions.

Equation (1) can be rearranged as

$$\frac{\rho_{\mathrm{CP}}^2 v_\infty^2 D^2}{\mu_{\mathrm{CP}}^2} = \mathrm{Re}_p^2 = \frac{8}{C_d}\frac{\rho_{\mathrm{CP}} D_0 \gamma}{\mu_{\mathrm{CP}}^2} = \frac{8}{C_d}\mathrm{Oh}_{\mathrm{CP}}^{-2}, \quad (2)$$

where we have introduced the CP Ohnesorge number $\mathrm{Oh}_{\mathrm{CP}} = \mu_{\mathrm{CP}}/\sqrt{\rho_{\mathrm{CP}} D_0 \gamma}$, which is a ratio of viscous and capillary time scales. Solving Eq. (2) for the droplet diameter is not trivial since Re_p and C_d depend on D. Careful examination of (2) reveals that Re_p at snap-off is independent of Ca and a function only of material properties and the pore size. Substituting the approximation $v_\infty = \frac{1}{2} D \frac{dv}{dz}$ and rearranging dimensionless groups yields

$$D/D_0 = \{(32/C_d)^{1/4}\mathrm{Oh}_{\mathrm{CP}}^{1/2}\}\mathrm{Ca}^{-1/2} = k\mathrm{Ca}^{-1/2}, \quad (3)$$

where we have introduced k for the prefactor in braces. The parameter k is nearly independent of Ca and depends almost entirely on CP properties, with the only DP contribution coming from the viscosity ratio λ. Because of the small exponents on C_d and $\mathrm{Oh}_{\mathrm{CP}}$, k varies little over a wide variety of fluid-fluid systems. This corresponds to the earlier mentioned square root scaling with shear rate, as $\mathrm{Ca} \propto \frac{dv}{dz}$.

For creeping flows $\mathrm{Re}_p < 1$, Eq. (3) can be solved by substituting the Hadamard and Rybczynski relation $C_d = [8(3\lambda + 2)/(1 + \lambda)]\mathrm{Re}_p^{-1}$ [14], which was derived for liquid spheres in translational motion (in the absence of a wall), canceling $\mathrm{Oh}_{\mathrm{CP}}$:

$$\frac{D}{D_0} = \left(\frac{2\lambda + 2}{3\lambda + 2}\right)^{1/2}\mathrm{Ca}^{-1/2}. \quad (4)$$

Thus, for small pores and slow flows, we can derive an exact force-balance expression for D/D_0. The Re_p in our experiments, however, ranges from $2 < \mathrm{Re}_p < 150$, so we solve Eq. (3) iteratively using an expression for C_d given by Saboni and Alexandrova [14] appropriate for our intermediate Re_p case, which amounts to a 35% correction in the drop diameter for the highest Re_p. Moreover, we compute the shear rate from our measured volumetric flow rate Q_{CP}, using an analytical solution by White [15], to derive the expression $\frac{dv}{dz} = 9.7 Q_{\mathrm{CP}}/H^{1.67}W^{1.33}$.

Figure 2(b) shows the Ca-dependent droplet size data, rescaled as $(1/k)D/D_0$. If our force balance were exact, the data would fall along the line $(1/k)D/D_0 = \mathrm{Ca}^{-1/2}$. This procedure does collapse the droplet size data, with a residual spread in normalized drop sizes of about 10% across all of the fluid systems studied. The collapsed data, however, fall systematically below the expected curve by about 20%. To investigate this discrepancy, we simulated the XME process using computational fluid dynamics [12,16]. The simulation results, also plotted in Fig. 2(b) with the symbol ☆, show excellent agreement with the experimental findings. Thus, the discrepancy is presumed due to the simplifying assumptions made in the force balance, e.g., neglecting the hydrodynamic effect of the membrane [17], assuming that the drag force acts perfectly antiparallel to the interfacial tension force, or neglecting neck effects similar to those in the dripping faucet [18]. To predict the XME droplet size *a priori*, one should use a value about 80% of that predicted by Eq. (3).

Next we construct phase diagrams that delimit where dripping and jetting occur as a function of We and Ca, shown in Figs. 3(a) and 3(c). We define jetting as occurring when the length of the neck L_n at snap-off exceeds the droplet diameter: $L_n/D > 1$, which correlates with large changes in D/D_0 over the range of Ca studied. A similar criterion is used in the dripping faucet literature [19]. At sufficiently low We and Ca, dripping is always observed, and, as either is increased, the behavior will eventually transition to jetting. Qualitatively, these phase diagrams exhibit the same form as those for coaxial liquid streams [5] and dripping faucets [20], at least when Ca is substituted for the Bond number Bo [11] in the latter case. In retrospect, one could have anticipated that jetting will occur whenever the force causing surface extension exceeds that causing surface contraction. This will happen independent of whether that force comes from the kinetic energy of the DP, the drag from the flowing CP, or gravity. The transition, however, does not occur at the same location in Ca-We space for all fluid systems; rather, it is also controlled by the DP Ohnesorge number $\mathrm{Oh}_{\mathrm{DP}} = \mu_{\mathrm{DP}}/\sqrt{\rho_{\mathrm{DP}} D_0 \gamma}$. Figure 3(b) shows how the transition

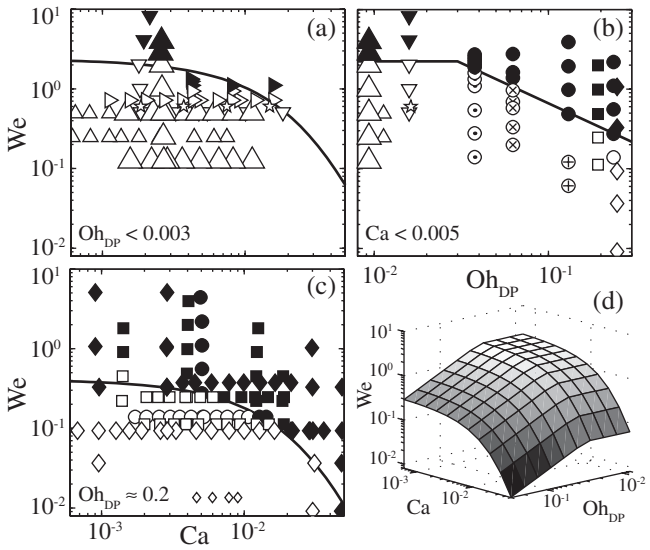

FIG. 3. Dripping to jetting phase behavior as a function of We, Ca, and $\mathrm{Oh}_{\mathrm{DP}}$. Dripping is indicated by open symbols, jetting by filled symbols. In (a) and (c), which plot the same region of Ca-We space at different $\mathrm{Oh}_{\mathrm{DP}}$, jetting is always seen at sufficiently high values of either We or Ca. The transition curve, shown by the solid lines, is a function of $\mathrm{Oh}_{\mathrm{DP}}$ and moves downward as $\mathrm{Oh}_{\mathrm{DP}}$ is increased. In (b), viewing the data in $\mathrm{Oh}_{\mathrm{DP}}$-We space highlights the $\mathrm{Oh}_{\mathrm{DP}}$ dependence (at low Ca). In (d), the surface separating dripping and jetting regimes, based on Eq. (5), is adapted from Refs. [19,20]. Jetting can also be observed below this surface if the predicted droplet size is $D/D_0 < 2$ (not shown). See Table I for symbol definitions.

varies in We-Oh_{DP} space at low Ca, and again we find remarkable similarity to what has been observed in the dripping faucet geometry [19].

In the dripping faucet, the separatrix between dripping and jetting has been determined. Clanet and Lasheras derived an analytical expression to describe the dripping-jetting transition in We-Bo space when $Oh_{DP} \to 0$ [20]. For finite Oh_{DP}, their expression quantitatively describes our low and high Oh_{DP} data when their We and Bo are replaced by a rescaled We and Ca, respectively, as shown by the solid lines in Figs. 3(a) and 3(c). Similarly, Ambravaneswaran *et al.* generated a phase diagram in We-Oh_{DP} space at fixed Bo through numerical simulations [19]; their data are reasonably well described by a two-segment piecewise power law in Oh_{DP} (corresponding to the inviscid and finite μ_{DP} limits). Again, this expression describes our data when Oh_{DP} is rescaled; the solid line in Fig. 3(b) shows this result. We find that the product of these two functions (with rescaled Ca and Oh_{DP}) describes our dripping-jetting transition surface in Ca-Oh_{DP}-We space:

$$\mathrm{We} = (c_1 \mathrm{Oh}_{\mathrm{DP}}^{-\alpha})\{1 + c_2 \mathrm{Ca}^2 - [(1 + c_2 \mathrm{Ca}^2)^2 - 1]^{1/2}\}^2, \quad (5)$$

where $c_2 = 860$, and $c_1 = 0.10$ and $\alpha = 0.89$ for $Oh_{DP} \geq 0.03$, or $c_1 = 2.27 = (0.10)(0.03)^{-0.89}$ and $\alpha = 0$ for $Oh_{DP} < 0.03$, as determined by least squares minimization. This surface is plotted in Fig. 3(d).

We also observe another dripping to jetting transition mechanism. Even at small Ca and We, under conditions where Eq. (3) predicts droplet sizes below the Rayleigh limit $D/D_0 \approx 2$, dripping gives way to a jet running tangent to the membrane, without apparently wetting it. In this case, the jet breaks up downstream to yield droplets of size $D/D_0 \approx 2$. This condition resembles operating conditions that prevail during emulsification in T junctions [7]. Taken with the preceding result, the (Ca, Oh_{DP}, We) triple appears sufficient to determine whether dripping or jetting will occur during any XME process.

Dripping, jetting, and the transition between them show remarkably similar characteristics in radically different geometries. Indeed, we were even able to adapt and analytically extend functional forms derived for the transition in faucets to the XME geometry with simple rescaling of the groups. Less surprisingly, the geometric details influence the relationship between droplet size and the relevant dimensionless groups. In the cross-flow membrane geometry as in the others, a force balance suffices for a precise prediction of droplet size as a function of process conditions. It seems likely that such relationships prevail in other microfluidic geometries as well. It remains unknown to what extent the lack of axisymmetry in our geometry affects the hydrodynamic singularity at the moment of snap-off [21] or how the process is modified by non-Newtonian fluid behaviors such as extensional elasticity [22].

We thank M. T. McClendon for developing the pendant drop profile analysis technique and W. B. Rogers for helpful discussions. This work was supported by Merck & Co., Inc.

*jcrocker@seas.upenn.edu

[1] J. Eggers, Rev. Mod. Phys. **69**, 865 (1997).
[2] L. Rayleigh, Proc. R. Soc. London **29**, 71 (1879).
[3] B. Ambravaneswaran, S. D. Phillips, and O. A. Basaran, Phys. Rev. Lett. **85**, 5332 (2000).
[4] P. Garstecki, M. J. Fuerstman, and G. M. Whitesides, Phys. Rev. Lett. **94**, 234502 (2005).
[5] A. S. Utada *et al.*, Phys. Rev. Lett. **99**, 094502 (2007).
[6] P. B. Umbanhowar, V. Prasad, and D. A. Weitz, Langmuir **16**, 347 (2000).
[7] S. van der Graaf *et al.*, Colloids Surf. A **266**, 106 (2005).
[8] A. J. Gijsbertsen-Abrahamse, A. van der Padt, and R. M. Boom, J. Membr. Sci. **230**, 149 (2004).
[9] S. M. Joscelyne and G. Tragardh, J. Membr. Sci. **169**, 107 (2000).
[10] I. Kobayashi *et al.*, AIChE J. **48**, 1639 (2002).
[11] The strength of the buoyancy force relative to the interfacial tension force is characterized by the Bond number $\mathrm{Bo} = \Delta\rho g D^2/\gamma$ and is negligible so long as $\mathrm{Bo} \ll 1$. In our experiments, $\mathrm{Bo} < 0.5$ in all cases.
[12] Computational fluid dynamics calculations were performed with the FLUENT 6.3 software package using the unsteady-state volume of fluid simulation scheme. Calculations were performed using a 6×10^5 cell grid with a symmetry plane dividing the space in two. Time steps were typically 10^{-5} s. The constant physical properties used were given in Table I. Boundary conditions were constant velocity at both inlets, constant pressure at the outlet, and a contact angle of 180° between the DP and the chamber walls.
[13] B. Song and J. Springer, J. Colloid Interface Sci. **184**, 64 (1996).
[14] A. Saboni and S. Alexandrova, AIChE J. **48**, 2992 (2002).
[15] F. M. White, *Viscous Fluid Flow* (McGraw-Hill, New York, 1974).
[16] A. J. Abrahamse *et al.*, AIChE J. **47**, 1285 (2001).
[17] M. E. O'Neill, Chem. Eng. Sci. **23**, 1293 (1968).
[18] W. D. Harkins and F. E. Brown, J. Am. Chem. Soc. **41**, 499 (1919).
[19] B. Ambravaneswaran *et al.*, Phys. Rev. Lett. **93**, 034501 (2004).
[20] C. Clanet and J. C. Lasheras, J. Fluid Mech. **383**, 307 (1999).
[21] I. Cohen *et al.*, Phys. Rev. Lett. **83**, 1147 (1999).
[22] P. E. Arratia *et al.*, Phys. Rev. Lett. **96**, 144502 (2006).